Development of tip-splitting and side-branching patterns in elastic fingering

João V. Fontana[1], Hermes Gadêlha[2], and José A. Miranda[1*]

[1] *Departamento de Física, Universidade Federal de Pernambuco,Recife, Pernambuco 50670-901 Brazil*
[2] *Department of Mathematics, University of York, York YO10 SDD, United Kingdom*

Elastic fingering supplements the already interesting features of the traditional viscous fingering phenomena in Hele-Shaw cells with the consideration that the two-fluid separating boundary behaves like an elastic membrane. Sophisticated numerical simulations have shown that under maximum viscosity contrast the resulting patterned shapes can exhibit either finger tip-splitting or side-branching events. In this work, we employ a perturbative mode-coupling scheme to get important insights into the onset of these pattern formation processes. This is done at lowest nonlinear order, and by considering the interplay of just three specific Fourier modes: a fundamental mode n, and its harmonics $2n$ and $3n$. Our approach further allows the construction of a morphology diagram for the system in a wide range of the parameter space without requiring expensive numerical simulations. The emerging interfacial patterns are conveniently described in terms of only two dimensionless controlling quantities: the rigidity fraction C, and a parameter Γ that measures the relative strength between elastic and viscous effects. Visualization of the rigidity field for the various pattern-forming structures supports the idea of an elastic weakening mechanism that facilitates finger growth in regions of reduced interfacial bending rigidity.

I. INTRODUCTION

The viscous fingering or Saffman-Taylor instability occurs when a fluid displaces another in the constrained environment of a Hele-Shaw cell [1], a device constituted by two parallel glass places separated by a narrow gap. This popular fluid dynamic instability is driven by the viscosity difference between the fluids that is quantified by the dimensionless viscosity contrast parameter

$$A = \frac{\mu_2 - \mu_1}{\mu_2 + \mu_1}, \qquad (1)$$

where μ_2 (μ_1) is the viscosity of the displaced (displacing) fluid, and $-1 \leq A \leq 1$. The instability takes place whenever the displaced fluid is more viscous (i.e., when $A > 0$). Under such circumstances, the interplay between (destabilizing) viscous effects and (stabilizing) surface tension forces leads to the formation of interfacial patterns presenting fingerlike shapes [2]. For radial fluid injection [3–9] the most prominent morphological feature of such patterns is the fact that the emerging fingers tend to bifurcate at their tips, generating the finger tip-splitting phenomenon. As a consequence, the evolving fingers tend to multiply and proliferate through repeated subdivisions, ultimately forming complex branched structures. It should be noted that the reverse flow case (where the more viscous fluid pushes the less viscous one, so that $A < 0$) as well as the viscosity-matched displacement (fluids presenting equal viscosities, implying that $A = 0$) do not produce any interfacial disturbances, so that the two-fluid separating boundary propagates in the form of a stable circular front.

During the past few years there has been a considerable interest in the study of reactive Hele-Shaw flows. In this type of fluid displacements the already interesting features of traditional viscous fingering phenomena [1, 2] are supplemented by the occurrence of chemical reactions at the fluid-fluid interface [10–19]. One particularly interesting experimental work on reactive Hele-Shaw flows has been performed by Podgorski *et al.* [19]. Their study focused on the usually stable viscous fingering situation involving the flow of two fluids of equal viscosities ($A = 0$), but induced the occurrence of chemical reactions at the interface. Surprisingly, instead of observing the evolution of stable concentric circular patterns, they detected the development of completely different interfacial morphologies presenting mushroom-shaped and tentaclelike structures. Curiously, no finger tip-splitting-type pattern has been found. The fact is that the chemical reaction induces the formation of an elastic gel-like layer between the fluids, so that the interfacial instabilities are not viscosity-driven, but triggered by the own elastic nature of the interface. This suggestive pattern-forming process defines the so-called elastic fingering instability.

The experimental elastic fingering results reported in [19] motivated additional work on this research topic, now addressing theoretical aspects of the problem [20, 21]. He *et al.* proposed a curvature weakening model that tried to reproduce the basic physics of the reactive flow system examined in [19]: they considered that the interface separating the fluids behaves as a thin elastic membrane, presenting a curvature-dependent bending rigidity whose value decreases as the local interfacial curvature κ increases [20]

$$\nu = \nu(\kappa) = \nu_0[Ce^{-\lambda^2 \kappa^2} + 1 - C]. \qquad (2)$$

In Eq. (2) ν_0 is the maximum rigidity that expresses the largest resistance to disturbances, and $0 \leq C < 1$ is the

bending rigidity fraction, which measures the fraction of intramolecular bonds broken through surface deformation. In addition, $\lambda > 0$ denotes a characteristic radius. One can think of the quantity $1/\lambda$ as being a characteristic curvature beyond which $\nu(\kappa)$ has a substantial decrease. Note that the constant bending rigidity limit is reached by setting $C = 0$. By deriving a modified Young-Laplace pressure jump condition, He and collaborators performed a linear stability analysis of the problem. Consistently with the experimental findings of Ref. [19], their linear results were able to account for the fact that the interface could become unstable even if the fluids have the same viscosity. However, their simple linear analysis was not able to extract any specific feature about the morphology of the emergent patterns.

Later, Carvalho and coworkers [21] utilized the curvature-dependent bending rigidity model proposed in [20] to carry out a weakly nonlinear analysis of the system, and showed that when $A = 0$ nonlinear effects play a crucial role to determine the general shape assumed by the resulting patterned structures [21]. Subsequently, the same group of researchers investigated the manifestation of elastic fingering in rotating Hele-Shaw cells, where still unexploited pattern-forming dynamic behaviors [22], and innovative stationary morphologies [23] have been revealed as a result of the competition between elastic and centrifugal forces.

Very recently, another theoretical work [24] revisited the elastic fingering problem, but focused on a different facet of it: contrary to what has been done in Refs. [19–21] which addressed the viscosity-matched $A = 0$ case, it analyzed the maximum viscosity contrast situation $A = 1$ in which a fluid of negligible viscosity displaces a fluid of finite viscosity. Recall that this is in fact the most common situation explored both theoretically and experimentally in the conventional viscous fingering problem [1–9]. Additionally, as opposed to Refs. [19–21] which examined early linear or weakly nonlinear time regimes, Ref. [24] concentrated on fully nonlinear time stages of the pattern formation dynamics. By using the curvature-dependent bending rigidity model, and employing state-of-the-art, extensive boundary integral numerical simulations, the authors of Ref. [24] have been able to unveil quite relevant information about the emerging patterns.

The cutting edge numerical results presented in [24] have shown that when viscous and elastic effects act simultaneously, one can get the rise of either finger tip-splitting (when $C = 0$), or side-branching (when $C = 0.5$) [see Fig. 5 in Ref. [24]]. During side-branching formation, interfacial lobes branch out sideways, forming dendriticlike patterns that resemble the shape of snowflakes. Even though the appearance of finger tip-splitting is not that surprising, the occurrence of side-branching is somewhat unexpected. After all, in the elastic fingering problem both fluids are Newtonian, but side-branching pattern formation in fluids normally arises in Hele-Shaw flows when the displaced fluid is non-Newtonian (shear-thinning) [25–32]. Therefore, it is worth pointing out
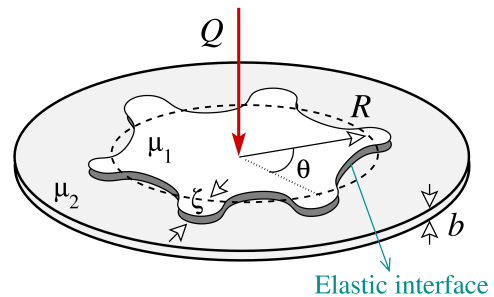

FIG. 1. (Color online) Representative sketch of a radial flow in a circular Hele-Shaw cell with an elastic interface (dark gray boundary) separating the inner fluid 1 and the outer fluid 2 (light gray region).

that in Ref. [24] the production of side-branching patterns is not related to the non-Newtonian nature of the fluids, but a result of the interplay between elastic and viscous effects.

In this work we examine the important maximum viscosity contrast ($A = 1$) situation investigated in Ref. [24], and try to assess their main numerical results regarding the morphology of the patterns via simple analytical means. This is done through the employment of a perturbative mode-coupling theory of the elastic fingering problem. We show that already at lowest nonlinear order, and by considering the coupling of just three specific Fourier modes, one can reproduce the onset formation of both finger tip-splitting and, most importantly the side-branching phenomena. A morphological diagram is proposed for the pattern formation problem, where the possible weakly nonlinear shapes are conveniently described in terms of two controlling dimensionless parameters: the rigidity fraction C and the quantity Γ which expresses the relative strength between elastic and viscous effects. Finally, the occurrence of the possible shapes is discussed in the light of an interfacial bending rigidity field, which is consistent with the weakening curvature effect proposed in Ref. [20] where interfacial elastic fingers arise more easily in regions of lower bending rigidity.

II. PHYSICAL PROBLEM AND GOVERNING EQUATIONS

Consider a circular Hele-Shaw cell of gap thickness b containing two immiscible, incompressible, Newtonian viscous fluids (see Fig. 1). Fluid 1 is injected into fluid 2 at a constant injection rate Q (equal to the area covered per unit time). Due to a chemical reaction there exists a gel-like interface separating the two fluids. As in Refs. [20–24] we treat the interface as an elastic membrane, presenting a curvature-dependent bending rigidity as given by Eq. (2). Notice that in this work we follow Ref. [24] and focus on the maximum viscosity contrast situation in which $\mu_2 \gg \mu_1$ such that $A \to 1$ in Eq. (1).

Within the scope of our mode-coupling weakly non-

linear analysis, the perturbed fluid-fluid interface is described as $\mathcal{R}(\theta, t) = R(t) + \zeta(\theta, t)$, where θ represents the azimuthal angle, and $R(t)$ is the time dependent unperturbed radius $R = R(t) = \sqrt{R_0^2 + Qt/\pi}$, with R_0 being the unperturbed radius at $t = 0$. Here, $\zeta(\theta, t) = \sum_{n=-\infty}^{+\infty} \zeta_n(t) \exp(in\theta)$ denotes the net interface perturbation with Fourier amplitudes $\zeta_n(t)$, and discrete wave numbers n. Our perturbative approach keeps terms up to the second-order in ζ. In the Fourier expansion of ζ we include the $n = 0$ mode to maintain the area of the perturbed shape independent of the perturbation ζ. Mass conservation imposes that the zeroth mode is written in terms of the other modes as $\zeta_0 = -(1/2R) \sum_{n\neq 0} |\zeta_n(t)|^2$.

For the quasi-two-dimensional configuration of the Hele-Shaw cell (very small gap thickness b), the flow is assumed to be potential [19–24]. Creeping flow would only result if the plates are farther apart (large b limit), which is not the case here. So, for our current small b situation, the gap-averaged flow velocity is $\mathbf{v}_j = -\boldsymbol{\nabla}\phi_j$, where ϕ_j represents the velocity potential in fluids $j = 1, 2$. The equation of motion of the interface is given by Darcy's law [1, 2, 20, 21]

$$A\left(\frac{\phi_1 + \phi_2}{2}\right) - \left(\frac{\phi_1 - \phi_2}{2}\right) = -\frac{b^2 \Delta p}{12(\mu_1 + \mu_2)}, \quad (3)$$

where

$$\Delta p = (p_1 - p_2)|_{r=\mathcal{R}} - (p_1 - p_2)|_{r=R}, \quad (4)$$

$(p_1 - p_2)|_{r=\mathcal{R}}$ denotes the pressure jump on the perturbed interface, and $(p_1 - p_2)|_{r=R}$ represents the pressure jump on the unperturbed interface. Similarly to what was done in [20, 21] the contributions coming from the elastic nature of the fluid-fluid interface are introduced via a generalized Young-Laplace pressure boundary condition, which expresses the pressure jump across the perturbed fluid-fluid interface as

$$(p_1 - p_2)|_{r=\mathcal{R}} = -\frac{1}{2}\nu'''\kappa^2\kappa_s^2 - \nu''\left(3\kappa\kappa_s^2 + \frac{1}{2}\kappa^2\kappa_{ss}\right)$$
$$- \nu'\left(\frac{1}{2}\kappa^4 + 3\kappa_s^2 + 2\kappa\kappa_{ss}\right)$$
$$- \nu\left(\frac{1}{2}\kappa^3 + \kappa_{ss}\right), \quad (5)$$

where the curvature-dependent bending rigidity $\nu = \nu(\kappa)$ is given by Eq. (2). In Eq. (5) the primes indicate derivatives with respect to the curvature κ, while the subscripts of κ indicate derivatives with respect to the arc length s.

To obtain a mode-coupling differential equation for the evolution of the perturbation amplitudes, first we define Fourier expansions for the velocity potentials, which obey Laplace's equation $\nabla^2\phi_j = 0$. Then, we express ϕ_j in terms of the perturbation amplitudes ζ_n by considering the kinematic boundary condition $\mathbf{n} \cdot \boldsymbol{\nabla}\phi_1 = \mathbf{n} \cdot \boldsymbol{\nabla}\phi_2$, which refers to the continuity of the normal velocity across the interface. Substituting these relations,

and the modified pressure jump condition Eq. (5) into Eq. (3), always keeping terms up to second-order in ζ, and Fourier transforming, yields the dimensionless mode-coupling equation (for $n \neq 0$) [8, 21]

$$\dot{\zeta}_n = \Lambda(n)\zeta_n$$
$$+ \sum_{m\neq 0}[F(n,m)\zeta_m\zeta_{n-m} + G(n,m)\dot{\zeta}_m\zeta_{n-m}], \quad (6)$$

where the overdot denotes total time derivative,

$$\Lambda(n) = \frac{1}{R^2}(A|n| - 1)$$
$$+ \frac{\Gamma}{2R^5}|n|(n^2 - 1)\left[A_1(C,\eta)(n^2 + 1) + A_2(C,\eta)\right], \quad (7)$$

is the linear growth rate,

$$\Gamma = \frac{b^2\nu_0\pi}{6(\mu_1 + \mu_2)Q\lambda^3} \quad (8)$$

measures the ratio of elastic to viscous forces,

$$A_1(C,\eta) = Ce^{-\eta}(-4\eta^2 + 10\eta - 2) - 2(1 - C), \quad (9)$$

$$A_2(C,\eta) = Ce^{-\eta}(8\eta^2 - 22\eta + 5) + 5(1 - C), \quad (10)$$

and $\eta = (1/R)^2$. We point out that $\Gamma = 1/\hat{J}$, where $\hat{J}$ is a parameter originally defined in Ref. [24].

The second-order mode-coupling terms are given by

$$F(n,m) = \frac{|n|}{R}\left\{\frac{A}{R^2}\left[\frac{1}{2} - \text{sgn}(nm)\right]\right.$$
$$- \frac{\Gamma Ce^{-\eta}}{R^5}\left[B_1(n,m) + \eta B_2(n,m)\right.$$
$$\left. + \eta^2 B_3(n,m) + 2\eta^3 B_4(n,m)\right],$$
$$\left. - \frac{\Gamma(1 - C)}{R^5}B_1(n,m)\right\}, \quad (11)$$

and

$$G(n,m) = \frac{1}{R}\left\{A|n|[1 - \text{sgn}(nm)] - 1\right\}, \quad (12)$$

where the sgn function equals ± 1 according to the sign of its argument. The expressions for the functions $B_1(n,m)$, $B_2(n,m)$, $B_3(n,m)$, and $B_4(n,m)$ are given in the appendix. Note that in Eqs. (6)-(12) lengths are rescaled by λ, and time by λ/U, where $U = Q/(2\pi\lambda)$ is a characteristic velocity. From this point onward we use the dimensionless version of all the equations. We stress that in this work, we focus on the important elastic fingering situation $A = 1$ in which the phenomena of finger tip-splitting and side-branching have been predicted numerically [24]. The set of equations (6)-(12) will be used to investigate analytically how these morphological features can be reproduced already at weakly nonlinear stages of the dynamics.
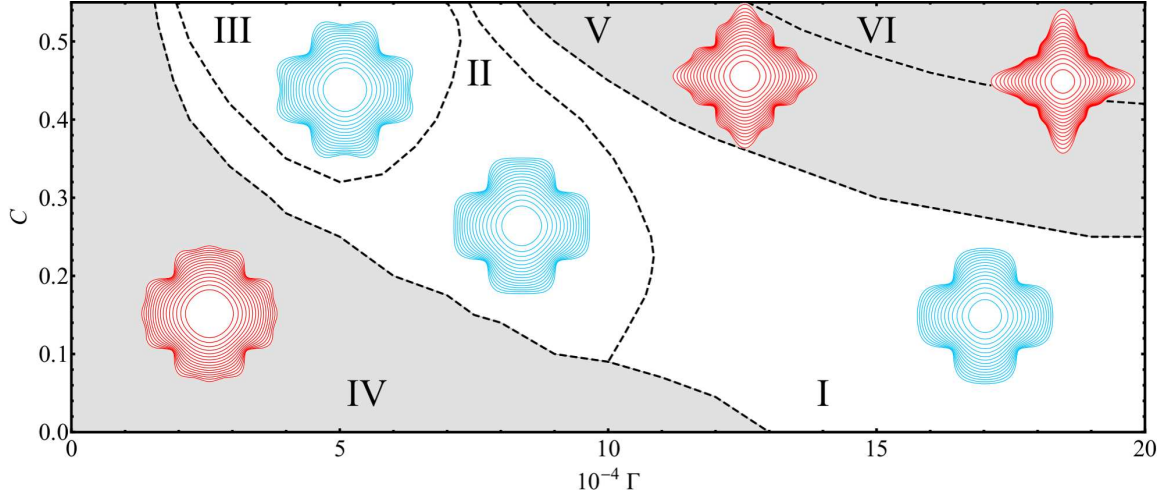
FIG. 2. (Color online) Elastic fingering morphology diagram in the parameter space (Γ, C). The dashed lines delimitate the boundaries separating six different morphological regions (I-VI). Regions I, II, and III are characterized by finger tip-broadening, finger tip-flattening, and finger tip-splitting, respectively. Conversely, regions IV, V, and VI present various manifestations of side-branching events.

III. ACCESS TO FINGER TIP-SPLITTING AND SIDE-BRANCHING VIA A WEAKLY NONLINEAR FORMULATION

A. Nonlinear fingering dynamics

By following Refs. [8, 30, 32], in order to address the onset of tip-splitting and side-branching events in the elastic fingering problem, we rewrite the net interface perturbation $\zeta(\theta, t)$ in terms of three specific cosine modes, namely the fundamental mode n, and its first and second harmonic modes $2n$ and $3n$

$$\zeta(\theta, t) = \zeta_0 \ + \ a_n(t)\cos(n\theta) \\ + \ a_{2n}(t)\cos(2n\theta) \ + \ a_{3n}(t)\cos(3n\theta), \quad (13)$$

where for a given mode $a_n(t) = \zeta_n(t) + \zeta_{-n}(t)$ denotes the real-valued cosine amplitude, and

$$\zeta_0 = -\frac{1}{4R(t)}\{[a_n(t)]^2 + [a_{2n}(t)]^2 + [a_{3n}(t)]^2\}. \quad (14)$$

Without loss of generality, as in Refs. [8, 30, 32] we choose the phase of the fundamental mode so that $a_n > 0$.

Within the scope of our second-order mode-coupling theory, finger tip-splitting, finger tip-broadening, and finger tip-narrowing are related to the influence of a fundamental mode n on the growth of its harmonic $2n$. It has been shown in Ref. [8] that an enhanced tendency of the fingers to get wider (narrower) occurs when $a_{2n} < 0$ ($a_{2n} > 0$). So, a negative growth for the cosine amplitude of the first harmonic mode $2n$ would mean tendency toward finger tip-splitting formation. A similar second-order mechanism refers to the side-branching phenomenon, and has been proposed in Refs. [30, 32]. In the realm of a mode-coupling model, it has been verified that

side-branching formation requires the presence of mode $3n$. If the harmonic mode amplitude a_{3n} is positive and sufficiently large, it can produce interfacial lobes branching out sidewards which we interpret as side-branching.

It is evident from Eqs. (13) and (14) that to describe the time evolution of the perturbed interface $\mathcal{R}(\theta, t) = R(t) + \zeta(\theta, t)$, one needs to know how the cosine amplitudes $a_n(t)$, $a_{2n}(t)$, and $a_{3n}(t)$ evolve in time. To do that, we rewrite the mode-coupling equation (6) in terms of cosine modes, considering the interplay of modes n, $2n$, and $3n$ to obtain

$$\dot{a}_n = \lambda(n) \ a_n + \frac{1}{2} \ \{[T(n, -n) + T(n, 2n)] \ a_n a_{2n} \\ + [T(n, 3n) + T(n, -2n)] a_{2n} a_{3n}\}, \quad (15)$$

$$\dot{a}_{2n} = \lambda(2n) \ a_{2n} + \frac{1}{2} \ \{T(2n, n) \ a_n^2 \\ + [T(2n, -n) + T(2n, 3n)] a_n a_{3n}\}, \quad (16)$$

and

$$\dot{a}_{3n} = \lambda(3n) \ a_{3n} + \frac{1}{2} \ [T(3n, n) + T(3n, 2n)] \ a_n a_{2n}, \quad (17)$$

where

$$T(n, m) = F(n, m) + \lambda(m)G(n, m). \quad (18)$$

For consistent second-order expressions, on the right hand side of Eqs. (15)-(17) we replaced time derivative terms like $\dot{a}_n$ by $\lambda(n) \ a_n$. The analytical solution for this type of differential equation has been given in Ref. [8] [see their Eq. (28), plus Eqs. (30)-(32)]. Of course, the time evolution of the amplitudes $a_n(t)$, $a_{2n}(t)$, and $a_{3n}(t)$ can also be readily obtained by numerically solving the coupled nonlinear differential equations (15)-(17).

B. Nonlinear pattern morphologies

We begin our discussion by presenting a morphology diagram for the onset of pattern formation in our elastic fingering system. Figure 2 depicts typical representative patterns by considering the parameter space (Γ, C). This diagram reveals that by varying the values of Γ and C one can identity six basic morphological regions: the first three regions (I, II, III) are related to the occurrence of finger tip-broadening (I), finger tip-flattening (II), and then finger tip-splitting (III). On the other hand, the remaining regions (IV, V, VI) are associated to the appearance of stubby side-branching shapes with pronounced finger broadening (IV), regular side-branching structures (V), and elongated side-branching patterns with stronger finger narrowing behavior. The dashed lines separating the various regions in Fig. 2 are obtained by inspecting the aspect of the resulting patterns while the governing parameters Γ and C are meticulously varied.

Our weakly nonlinear morphology diagram contemplates the possibility of existence of tip-splitting and closely related events (regions I, II, and III), plus the prevalence of side-branching phenomena (regions IV, V, and VI)), being consistent with the sophisticated numerical results reported in Ref. [24]. This can be verified by inspecting the early time stages of the numerical simulations shown in Fig. 5 of Ref. [24], and comparing them with the weakly nonlinear patterns shown in Fig. 2. Note that in contrast to what has been done in [24], instead of focusing only on two values of the rigidity fraction C (namely, $C = 0$ and $C = 0.5$), we exploited the values of C for which the elastic fingering instability develops, keeping the linear growth rate positive and bound [20]. In addition, we also have sweeped out the characteristic values of the parameter Γ, within the range $0 < \Gamma \leq 20 \times 10^{-4}$ (Fig. 5 in [24] only considers $\Gamma = 1/230 \approx 43, 4 \times 10^{-4}$). It should be stressed that we have carefully searched for other families of patterns within and beyond the range of parameters C and Γ considered in Fig. 2, within an empirically relevant parameter regime, but have not found any other dramatically distinct type of patterned morphologies than the ones presented here.

At this point, it should be noted that as in Refs. [33, 34], while plotting the evolving interfaces shown in Fig. 2 and in the remaining figures of this work, we stop the time evolution of the patterns as soon as the base of the fingers starts to move inwards, which would make successive interfaces cross one another. Since this crossing is not observed in experiments [3–7] and simulations [9, 24], we adopt the largest time before crossing as the upper bound time $(t = \tau)$ for the validity of our theoretical description. This validity condition can be mathematically expressed as

$$\left[\frac{d\mathcal{R}}{dt}\right]_{t=\tau} = [\dot{R}(t) + \dot{\zeta}(\theta, t)]_{t=\tau} = 0. \qquad (19)$$

Notice that, differently from what has been done in Ref. [34] we evaluate Eq. (19) by taking into account second-order contributions for interface perturbation $\zeta(\theta, t)$, as prescribed by our mode-coupling equation (6).

To better appreciate the weakly nonlinear behaviors expressed by the typical pattern-forming structures shown in regions I, II, and III in Fig. 2, we examine them more closely in Fig. 3. On the top of each panel, we depict the fluid-fluid interface evolution considering the interaction of three representative cosine modes ($n = 4$, $2n = 8$, and $3n = 12$). On the bottom part of the panels, we plot the corresponding time evolution of the rescaled cosine amplitudes $a_n(t)/R(t)$ for each of these cosine modes. This is done for regions: (a) I, (b) II, and (c) III. Similar kind of plots are presented in Fig. 4 for the side-branching regions IV, V, and VI. We stress that all patterns illustrated in Figs. 2-5 have the same the initial amplitudes at $t = 0$ s $a_n(0) = R_0/80$, where $R_0 = 1.5$, and $a_{2n}(0) = a_{3n}(0) = 0$ so that modes $2n$ and $3n$ are both initially absent. This is done to avoid artificial growth of modes a_{2n} and a_{3n} imposed solely by the initial conditions. This way, the phenomenon of finger tip-splitting and side-branching we study are spontaneously induced by the weakly nonlinear dynamics, and not by artificially imposing large initial amplitudes for a_{2n} and a_{3n}. Moreover, $0 \leq t \leq \tau$, where for each case the final time τ is obtained from Eq. (19). Even though all the patterns depicted in Figs. 2-5 have the same initial conditions, the innermost interface taken at $t = 0$ may appear to differ in size from plot to plot. This happens because the sizes of some of the shapes have been slightly modified to allow better visualization of their morphological features.

By inspecting Fig. 3(a) for region I (small C and large Γ), we see a nearly circular initial interface evolving to a four-fingered structure. Note that it is the growth of the fundamental mode $n = 4$ that sets the initial n-fold symmetry for the pattern. Finger tip-widening can be observed as time progresses, but the finger tips still present a rounded shape. The broadening of the finger tips is justified by the growth of the negative first harmonic mode $2n$ ($a_{2n} < 0$). On the other hand, the pattern shown in Fig. 3(b) for region II (intermediate values of C and Γ) present fingers that are wider than those shown in Fig. 3(a), and now the finger tips become increasingly flat. This finger tip-flattening behavior is chiefly due to the increased growth of the negative first harmonic mode. Then, by observing Fig. 3(c) for region III (large C and small Γ) we finally see the occurrence of the finger tip-splitting phenomenon (resulting in typical flowerlike patterns) mainly induced by the enhanced growth of mode $2n$. It is worth noting that the amplitude of the mode $3n$ is very small in regions I, II, and III so that side-branching formation is not favored there. However, the small (but non-negligible) growth of the harmonic amplitude $a_{3n} > 0$ in regions I and II acts to delay the formation of tip-splitting in these regions. One can say that regions I, II, and III involve patterned structures that eventually tend to evolve into a finger tip-splitting configuration. It is well known from experiments [3–7] and
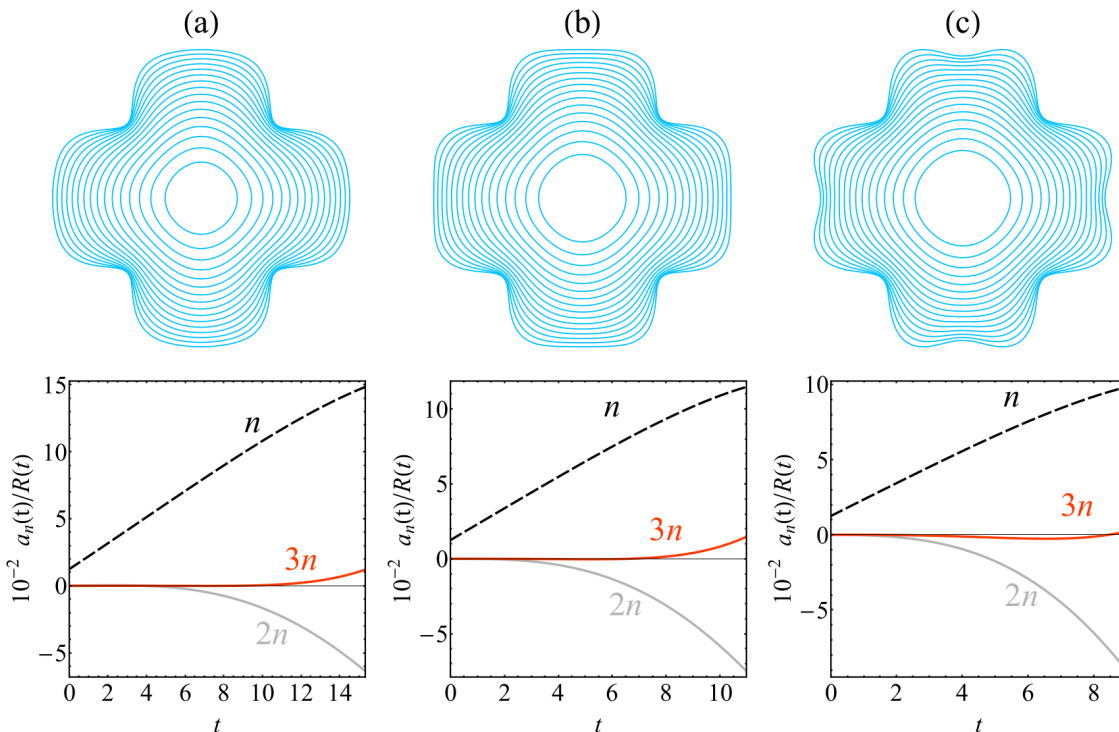
FIG. 3. (Color online) Representative elastic fingering patterns of regions I, II, and III (top panel), and the corresponding time evolution of the rescaled cosine amplitudes $a_n(t)/R(t)$ for modes $n = 4$, $2n = 8$, and $3n = 12$ (bottom panel). The values of the controlling dimensionless parameters utilized in each of the regions are: (a) $C = 0.25$, $\Gamma = 20 \times 10^{-4}$, $\tau = 15.33$; (b) $C = 0.35$, $\Gamma = 8 \times 10^{-4}$, $\tau = 10.97$; (c) $C = 0.55$, $\Gamma = 4 \times 10^{-4}$, $\tau = 9.01$.

fully nonlinear numerical simulations [2, 9, 24, 28] that the phenomenon of finger tip-splitting is always preceded by the occurrence of finger tip-broadening and flattening. It is also worthwhile to note that if we use the values of the relevant parameters that have been utilized in the numerical simulations of Fig. 5(a) of Ref. [24] (i.e, $\Gamma = 1/230 \approx 43, 4 \times 10^{-4}$, $C = 0$, $R_0 = 1$, and $a_n(0) = R_0/100$) we obtain a weakly nonlinear pattern belonging to region I, consistently with the early time interfacial morphology detected in [24].

Now we turn our attention to Fig. 4 and focus on the basic morphologies and dynamical responses associated to regions IV, V, and VI. The most evident observation is that the patterned structures depicted in Fig. 4 are quite different from the shapes shown in Fig. 3. For instance, in regions IV, V, and VI there is no sign of finger tip-splitting events. On the contrary, it is clear from Fig. 4 that the most prevalent mechanism is now side-branching. In Fig. 4(a) for region IV (small C and small Γ) we see the development of an initially fourfold structure which evolves towards a twelve-folded fingered morphology, clearly showing the presence and growth of a sizable mode amplitude $a_{3n} > 0$. Recall that a positive sign for a_{3n} favors side-branching formation. However, it can also be noticed that the mode amplitude $a_{2n} < 0$, a sign that would favor finger widening. As a result of the competition between modes $2n$ and $3n$ a stubby side-

branched pattern arises in region IV, where the fingers are relatively wide but branch-out sideways. The stubby nature of this particular pattern is partially due to the somewhat restrained growth of the fundamental mode n. A different situation is illustrated in Fig. 4(b) for region V (large C and intermediate Γ): now we have the sizable growth of positive mode amplitude $a_{3n} > 0$ acting in conjunction with a more moderate growth of a positive mode amplitude $a_{2n} > 0$ (a sign that would favor finger narrowing). As a consequence, a more characteristic finger side-branching structure arises in region V. Finally, in Fig. 4(c) for region VI (large C and large Γ) we still observe a sizable $a_{3n} > 0$, but now accompanied by a even larger $a_{2n} > 0$, producing the formation of side-branching shapes presenting long and narrow finger tips. Once again, if we set the parameters as in Ref. [24] ($\Gamma = 1/230 \approx 43, 4 \times 10^{-4}$, $C = 0.5$, $R_0 = 1$, and $a_n(0) = R_0/100$) we obtain a weakly nonlinear pattern belonging to region VI, in line with what is observed at initial times in Fig. 5(b) of [24].

The weakly nonlinear morphology diagram presented in Fig. 2 also raises an important question on how transitions from side-branching (region IV) to tip-splitting-type behavior (regions I-III), and then again back to side-branching (regions V and VI) happen as the two controlling parameters C and Γ are increased. The mechanism by which these transitions take place is related to com-
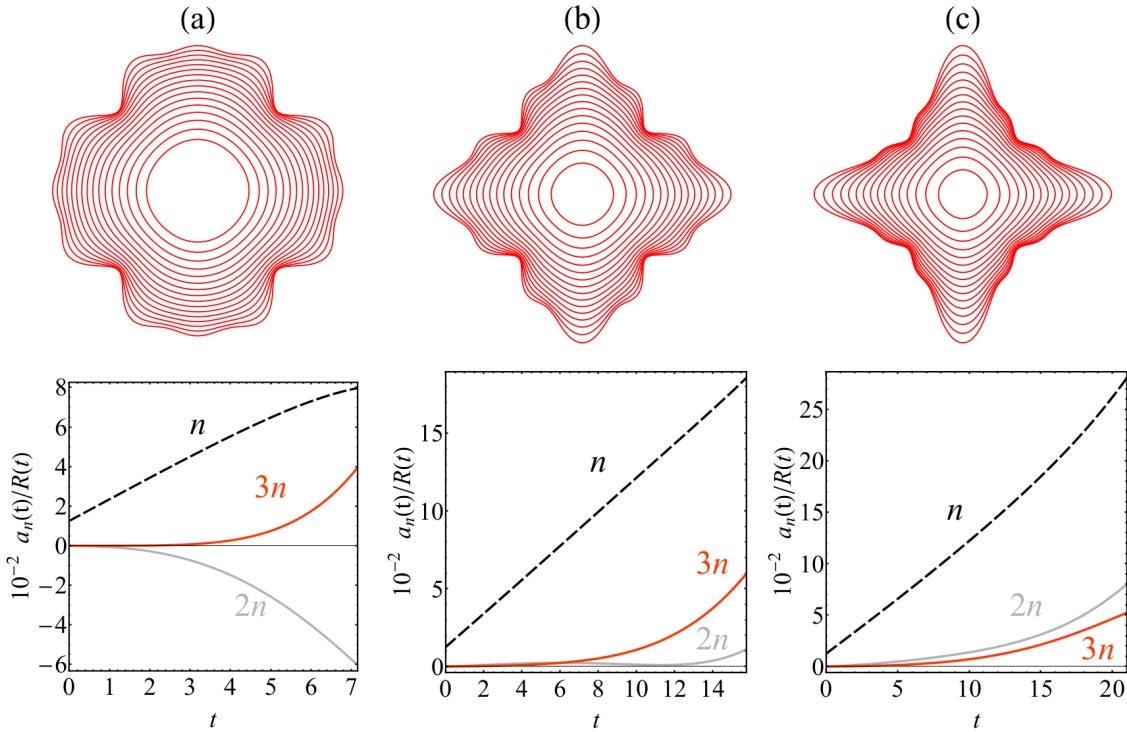
FIG. 4. (Color online) Representative elastic fingering patterns of regions IV, V, and VI (top panel), and the corresponding time evolution of the rescaled cosine amplitudes $a_n(t)/R(t)$ for modes $n = 4$, $2n = 8$, and $3n = 12$ (bottom panel). The values of the controlling dimensionless parameters utilized in each of the regions are: (a) $C = 0.15$, $\Gamma = 1.5 \times 10^{-4}$, $\tau = 7.15$; (b) $C = 0.55$, $\Gamma = 11 \times 10^{-4}$, $\tau = 15.78$; (c) $C = 0.50$, $\Gamma = 15 \times 10^{-4}$, $\tau = 21.02$.

plex mode-coupling interactions via a dynamical system expressed by Eqs. (15)-(17), which stability, transitions and bifurcation depend on complicated mode-coupling functions [Eqs. (7)-(12)] on a three-dimensional parameter space (C, Γ, A), and thus fairly challenging to rationalize. At this point, we do not have a simple physical explanation for this. We hope future analytical, numerical, or experimental studies of elastic fingering in Hele-Shaw cells will further address such an open question.

In order to better understand the role of the bending weakening effect of the elastic interface while developing tip-splitting and side-branching morphologies, we depict in Fig. 5 the associated time evolution of the bending rigidity field for the observed patterns in Figs. 3 and 4. The shape-dependence of the bending rigidity entails dynamical changes expressed by Eq. (2) as the interface evolves in time $(0 \leq t \leq \tau)$. For a given time, we plot how the function $\nu(t)/\nu_0$ varies along the fluid-fluid interface: since the curvature varies along the boundary, the quantity $\nu(t)/\nu_0$ also changes along the interface. Such changes are expressed by the color coding utilized in Fig. 5: lower values of $\nu(t)/\nu_0$ are represented by dark colors, while larger values of $\nu(t)/\nu_0$ are associated to lighter colors. The resulting bending rigidity field patterns depicted in Fig. 5 are obtained by overlaying the time series of $\nu(t)/\nu_0$ along the associated expanding interface at each computed time. Figure 5 shows that this spatial-temporal dynamics of the bending rigidity for the tip-splitting Fig. 5(a)-Fig. 5(c) and side-branching Fig. 5(d)-Fig. 5(f) phenomena are remarkably distinct. In Figs. 5(a)-5(c) the weakening of the interfacial bending rigidity can be traced back to early stages of the dynamics, with finger tip-splitting instigated by a sudden increase of the bending rigidity at the tip of the finger. Note however that this increase in bending rigidity does not need be large, and indeed a small increase in the bending stiffness is sufficient to suppress local curvature growth, thus instigating the finger with already reduced rigidity to split.

In contrast, the elastically induced side-branching phenomena in Figs. 5(d)-5(f) are weakly correlated to early stages of the dynamics. Although in this case, the side-branching morphology is equally influenced by the dynamical decrease of the bending rigidity field, which can be reduced by more than half of its maximum value, large bending rigidity magnitudes are held for longer periods. As a result, finger side-branching is delayed until the bending rigidity field is sufficiently weakened to allow the instability to grow. The latter can be clearly observed by comparing the relatively large region of increased bending rigidity in Fig. 5(f) as opposed to Fig. 5(c). Furthermore, the mechanism behind the elastic finger side-branching formation presented in Fig. 5 has similarities with the side-branching phenomena observed, instead, in
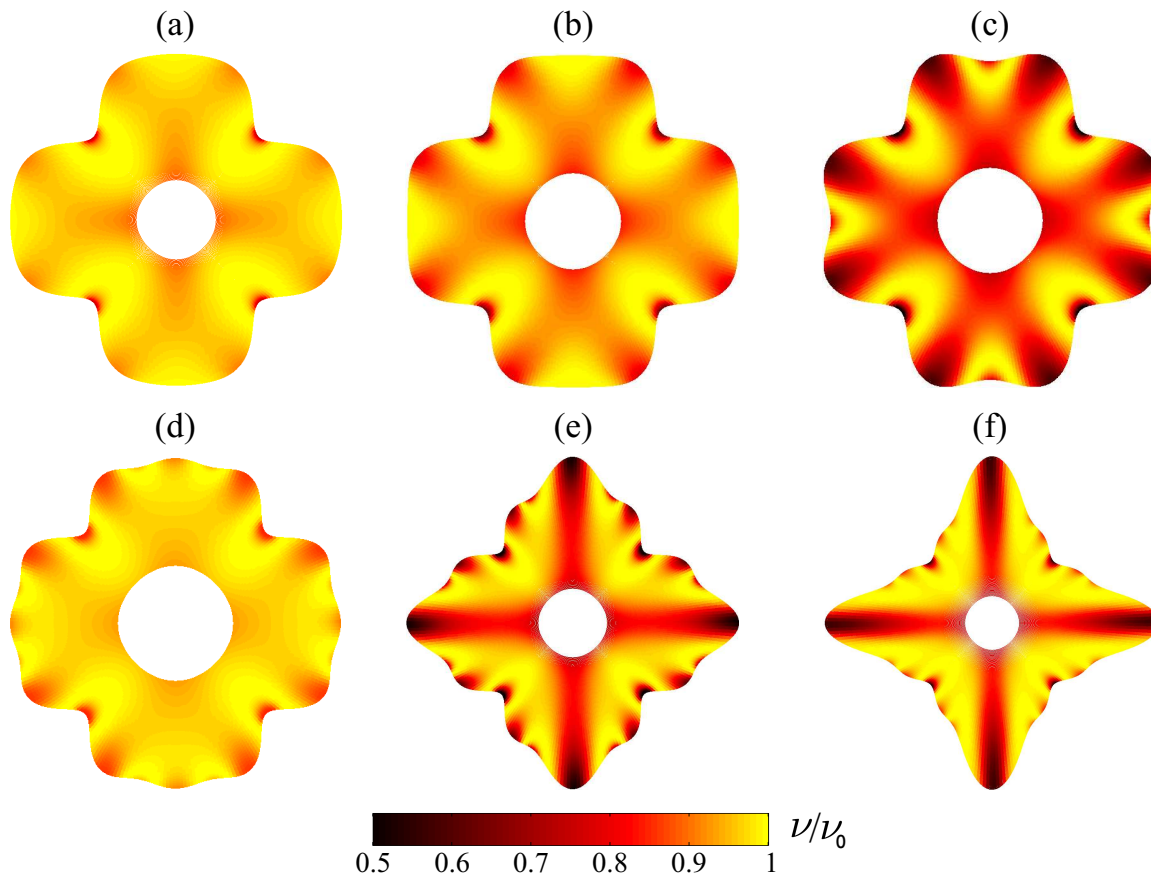
FIG. 5. (Color online) Time evolution of the dimensionless rigidity field ν/ν_0 for the evolving interfaces illustrated in the top panels of Figs. 3 and 4: (a)-(c) tip-splitting related regions; (d)-(f) side-branching regions.

shear-thinning fluids [25–32]. While for the latter, the viscous resistance decreases with the flow rate, here the interfacial elastic bending resistance is reduced with the local curvature. Incidentally, in Hele-Shaw pattern forming structures the regions of large fluid displacement also instigate growth of interfacial curvatures, thus there is phenomenological overlap between these two very distinct systems.

Our current analytical study complements the numerical work of Ref. [24] in the sense that the used perturbative scheme allows one to explore the whole phase diagram for morphological changes, whereas the boundary integral method utilized in [24] is quite expensive, and not exactly easy to explore the whole phase diagram. However, it should also be noted that the current work only addresses the initial stages of the instability (at the onset of nonlinearities), while Ref. [24] brings to light the entire dynamic evolution of the system (both initial, intermediate, and fully nonlinear stages of the flow).

IV. CONCLUDING REMARKS

An interesting experimental study on reactive Hele-Shaw flow performed by Podgorski *et al.* [19] has demonstrated that visually striking fingering structures arise at the fluid-fluid boundary (e.g., mushroom-shaped and tentaclelike patterns), even if the fluids involved have the same viscosity. This fact motivated He and coworkers [20] to introduce the notion of elastic fingering, in which interfacial disturbances are not induced by the viscosity difference between the fluids, but are produced by the own elastic nature of a gel-like separating layer. Their weakening curvature model treated the two-fluid interface as an elastic membrane presenting a curvature-dependent bending rigidity, and was able to predict the development of interfacial instabilities even in the viscosity-matched case ($A = 0$). Very recently, Zhao and collaborators [24] revisited the elastic fingering problem, and used sophisticated numerical simulations to analyze the pattern formation scenario when both elastic and viscous effects act simultaneously. Their elegant numerical results indicated that, under maximum viscosity contrast circumstances ($A = 1$), one can obtain the emergence of either tip-splitting or side-branching morphologies.

Inspired by the appealing fully nonlinear numerical findings presented in Ref. [24], in this work we complement their study by examining the weakly nonlinear stages of the pattern-forming dynamics through analytic means. Our main purpose was to gain useful insights into

the possible physical mechanisms leading to the uprising of finger tip-splitting and side-branching phenomena during elastic fingering. We have shown that by implementing a second-order mode-coupling theory, and considering the interplay of just a few Fourier modes (a fundamental mode n, and its harmonics $2n$ and $3n$) one is able to capture the most prominent morphological features leading to both tip-splitting (enhanced growth of harmonic amplitudes $a_{2n} < 0$) and side-branching (favored growth of harmonic amplitudes $a_{3n} > 0$) formation. A weakly nonlinear morphology diagram is provided for the system, being conveniently described by just two controlling dimensionless quantities: the rigidity fraction C, and a parameter Γ that measures the competition between elastic and viscous effects. Such a morphology diagram is especially useful to provide an understanding of the parametric conditions required to suppress finger tip-splitting events, and replace them by fingers that side-branch from their tips. Construction of a dimensionless rigidity field for the various possible emerging patterns reinforces the importance weakening curvature effect [20], in the sense that the occurrence of fingering is favored in regions of lower interfacial rigidity.

We are not aware of any existing experimental studies for the elastic fingering problem with $A = 1$. To the best of our knowledge, the only existing experiments of the problem focused on the viscosity matched case $A = 0$, and has been presented in Ref. [19]. However, after the publication of the fully nonlinear numerical simulations recently presented in Ref. [24], and of our current analytical weakly nonlinear study, we do hope that experimentalists will feel motivated to verify our theoretical, pattern-forming predictions.

In their recent numerical work, Zhao *et. al* [24] have shown that depending on the parameters and the initial conditions, the patterns can reach a self-similar state or evolve to a limiting shape for which the elasticity of the interface is not important. These effects are illustrated in Figs. 6 and 7 of Ref. [24]. However, our current second-order weakly nonlinear results do not predict such

stabilization processes.

Appendix: Functions appearing in the mode-coupling term $F(n,m)$

This appendix presents the expressions for the functions $B_1(n,m)$, $B_2(n,m)$, $B_3(n,m)$, and $B_4(n,m)$ which appear in Eq. (11) of the text

$$
\begin{aligned}
B_1(n,m) = & -3 + \frac{15}{4}m(n-m) + 10(n-m)^2 \\
& - \frac{9}{2}m^2(n-m)^2 - 6m(n-m)^3 \\
& - 4(n-m)^4,
\end{aligned} \tag{A.1}
$$

$$
\begin{aligned}
B_2(n,m) = & \frac{39}{2} - 30m(n-m) - 71(n-m)^2 \\
& + \frac{81}{2}m^2(n-m)^2 + 54m(n-m)^3 \\
& + 32(n-m)^4 - 12m^2(n-m)^4 \\
& - 12m^3(n-m)^3,
\end{aligned} \tag{A.2}
$$

$$
\begin{aligned}
B_3(n,m) = & -14 + 25m(n-m) + 54(n-m)^2 \\
& - 36m^2(n-m)^2 - 48m(n-m)^3 \\
& - 26(n-m)^4 + 18m^2(n-m)^4 \\
& + 18m^3(n-m)^3,
\end{aligned} \tag{A.3}
$$

and

$$
\begin{aligned}
B_4(n,m) = & 1 - 2m(n-m) - 4(n-m)^2 \\
& + 3m^2(n-m)^2 + 4m(n-m)^3 \\
& + 2(n-m)^4 - 2m^2(n-m)^4 \\
& - 2m^3(n-m)^3.
\end{aligned} \tag{A.4}
$$

[1] P. G. Saffman and G. I. Taylor, Proc. R. Soc. London Ser. A **245**, 312 (1958).

[2] For review papers, see G. M. Homsy, Annu. Rev. Fluid Mech. **19**, 271 (1987); K. V. McCloud and J. V. Maher, Phys. Rep. **260**, 139 (1995); J. Casademunt, Chaos **14**, 809 (2004).

[3] L. Paterson, J. Fluid Mech. **113**, 513 (1981).

[4] H. Thomé, M. Rabaud, V. Hakim, and Y. Couder, Phys. Fluids A **1**, 224 (1989).

[5] J.-D. Chen, J. Fluid Mech. **201**, 223 (1989); J. -D. Chen, Exp. Fluids **5**, 363 (1987).

[6] S. S. S. Cardoso and A. W. Woods, J. Fluid Mech. **289**, 351 (1995).

[7] O. Praud and H. L. Swinney, Phys. Rev. E **72**, 011406 (2005).

[8] J. A. Miranda and M. Widom, Physica D **120**, 315 (1998).

[9] S. W. Li, J. S. Lowengrub, and P. H. Leo, J. Comput. Phys. **225**, 554 (2007).

[10] Y. Nagatsu, Curr. Phys. Chem. **5**, 52 (2015).

[11] F. Haudin and A. De Wit, Phys. Fluids **27**, 113101 (2015).

[12] F. Haudin, J. H. E. Cartwright, and A. De Wit, Proc. Nat. Acad. Sc. U.S. A. **111**, 17363 (2014).

[13] Y. Nagatsu, Y. Ishii, Y. Tada, and A. De Wit, Phys. Rev. Lett. **113**, 024502 (2014).

[14] A. De Wit, K. Eckert, and S. Kalliadasis, Chaos **22**, 037101 (2012).

[15] C. Almarcha, P.M.J. Trevelyan, P. Grosfils, and A. De Wit, Phys. Rev. Lett. **104**, 044501 (2010).

[16] M. Mishra, P.M.J. Trevelyan, C. Almarcha, and A. De Wit, Phys. Rev. Lett. **105**, 204501 (2010).

[17] L. A. Riolfo, Y. Nagatsu, S. Iwata, R. Maes, P.M.J. Trevelyan, and A. De Wit, Phys. Rev. E **85**, 015304(R) (2012).

[18] L. A. Riolfo, J. Carballido-Landeira, C. O. Bounds, J. A. Pojman, S. Kalliadasis, and A. De Wit, Chem. Phys. Lett. **534**, 13 (2012).

[19] T. Podgorski, M. C. Sostarecz, S. Zorman, and A. Belmonte, Phys. Rev. E **76**, 016202 (2007).

[20] A. He, J. S. Lowengrub, and A. Belmonte, SIAM J. Appl. Math. **72**, 842 (2012).

[21] G. D. Carvalho, J. A. Miranda, and H. Gadêlha, Phys. Rev. E **88**, 053006 (2013).

[22] G. D. Carvalho, H. Gadêlha, and J. A. Miranda, Phys. Rev. E **89**, 053019 (2014).

[23] G. D. Carvalho, H. Gadêlha, and J. A. Miranda, Phys. Rev. E **90**, 063009 (2014).

[24] M. Zhao, A. Belmonte, S. Li, and J. S. Lowengrub, J. Comp. Appl. Math. (to appear), http://dx.doi.org/10.1016/j.cam.2015.11.016.

[25] A. Buka, P. Palffy-Muhoray, and Z. Racz, Phys. Rev. A **36**, 3984 (1987).

[26] H. Zhao and J. V. Maher, Phys. Rev. E **47**, 4278 (1993).

[27] L. Kondic, P. Palffy-Muhoray, and M. J. Shelley, Phys. Rev. E **54**, R4536 (1996).

[28] L. Kondic, M. J. Shelley, and P. Palffy-Muhoray, Phys. Rev. Lett. **80**, 1433 (1998).

[29] P. Fast, L. Kondic, M. J. Shelley, and P. Palffy-Muhoray, Phys. Fluids **13**, 1191 (2001).

[30] M. Constantin, M. Widom, and J. A. Miranda, Phys. Rev. E **67**, 026313 (2003).

[31] P. Fast and M. J. Shelley, J. Comput. Phys. **195**, 117 (2004).

[32] J. V. Fontana, S. A. Lira, and J. A. Miranda, Phys. Rev. E **87**, 013016 (2013).

[33] E. O. Dias and J. A. Miranda, Phys. Rev. E **81**, 016312 (2010).

[34] M. J. P. Gringras and Z. Rácz, Phys. Rev. A **40**, 5960 (1989).